



**HAL**  
open science

## Crater jet morphology

Sarah Badr, Georges Gauthier, Philippe Gondret

► **To cite this version:**

Sarah Badr, Georges Gauthier, Philippe Gondret. Crater jet morphology. *Physics of Fluids*, 2016, 28 (3), pp.033305. 10.1063/1.4943160 . hal-04009370

**HAL Id: hal-04009370**

**<https://hal.science/hal-04009370>**

Submitted on 10 Mar 2024

**HAL** is a multi-disciplinary open access archive for the deposit and dissemination of scientific research documents, whether they are published or not. The documents may come from teaching and research institutions in France or abroad, or from public or private research centers.

L'archive ouverte pluridisciplinaire **HAL**, est destinée au dépôt et à la diffusion de documents scientifiques de niveau recherche, publiés ou non, émanant des établissements d'enseignement et de recherche français ou étrangers, des laboratoires publics ou privés.

## Crater jet morphology

Sarah Badr,<sup>1</sup> Georges Gauthier,<sup>1, a)</sup> and Philippe Gondret<sup>1, b)</sup>

*Laboratoire FAST, Univ. Paris-Sud, CNRS, Université Paris-Saclay, F-91405,  
Orsay, France*

(Dated: 4 January 2016)

We present a detailed analysis of the morphology of craters induced by a round gas jet impinging vertically onto horizontal non-cohesive granular bed. The virtual origin of the jet from a self-similar model is taken into account both in the size scaling of the craters and in the inertial Shields number that governs the erosive processes. Two intrinsic types of craters with different morphologies are found and characterized in detail from shallow parabolic craters (type I) to deep conical craters (type II). whereas a flat central part arises from a finite bed thickness and leads to truncated morphologies. The transitions between the different crater morphologies are also analyzed in detail. The local Shields number based on the local velocity at the evolving bed surface is shown to depend on the local crater shape at the impinging point of the jet.

---

<sup>a)</sup>Electronic mail: [gauthier@fast.u-psud.fr](mailto:gauthier@fast.u-psud.fr)

<sup>b)</sup>Electronic mail: [gondret@fast.u-psud.fr](mailto:gondret@fast.u-psud.fr)

## I. INTRODUCTION

Erosion is encountered in numerous natural or industrial situations. Understanding erosion process is essential for instance to interpret geomorphological patterns on Earth or other planets and to predict the evolution of estuaries and river beds.<sup>1</sup> In nuclear power industry, the cleaning of high radioactive product tanks is performed by eroding materials laying on the bottom of the tank.<sup>2</sup> But erosion could arise spontaneously during a reactor overheating which may lead to the spreading of radioactive materials in the primary circuit of the reactor.<sup>3</sup> Predicting and eventually preventing erosion is thus a major key for the safety of nuclear reactors.<sup>4</sup> Finally, erosion is the main cause of dam and embankment failure<sup>5</sup> so that the direct knowledge of soil stability, which requires reliable in situ measurements, is necessary for risk prevention. The Jet Erosion Test (JET) proposed by Hanson and Cook,<sup>6</sup> following the work of Mazurek *et al.*<sup>7</sup> and references herein, has been developed for this final purpose. JET consists in the measurements of the mass and depth cratering by a strong impinging water jet which gives access to an erodibility coefficient and the critical shear stress of the soil.

Craters eroded by impinging jets exhibit different morphologies from simple hemispheric or parabolic shapes to more complicated shapes with mixed curved and straight parts.<sup>8-13</sup> The origin of these different shapes and their detailed link with the soil properties and the jet flow remains however unclear. The difficulty arises from the complex hydrodynamics of the spatially evolving jet flow and from the strong coupling with the deformable soil. The spatial evolution of the jet can be divided into successive regions from the nozzle exit with a free-jet behavior towards its interaction with the soil : (i) the potential core close to the nozzle exit where the jet axial velocity remains constant together with a spatially evolving mixing layer, (ii) the downstream free-jet region where the decaying axial velocity and increasing transverse width of the jet may be described by self-similar models arising from a virtual point origin and with conservation arguments, (iii) the *impinging jet region* at the soil where the streamlines are sharply curved close to one stagnation point, which is a high pressure region of radial gaussian extension, and (iv) the wall-jet region where the flow is mainly parallel to the soil with a radially decreasing shear stress. Even in the absence of soil interaction, the description of free jets with self-similar models remains complex and may work satisfactorily only within some downstream regions of limited extension.<sup>14</sup> Besides, the

interaction with the soil is not very clear and several erosion processes have been imagined from the so-called “Viscous Erosion” to the “Diffusion-Driven flow”.<sup>12</sup> Therefore, there is a need of new well controlled experiments with model soils together with numerical simulations that take into account its inherent discrete nature.<sup>13,15,16</sup>

Erosion and mass transport are commonly described using either the Shields number that compares the driving hydrodynamic force to the resisting apparent weight of one grain, or the Rouse number that compares the flow velocity to the settling velocity of one grain. Since pioneering works,<sup>8,17</sup> the Shields number is mainly used for bedload transport whereas the Rouse number is usually used in general for suspension transport. However, both numbers are linked through the particle Reynolds number that gives the hydrodynamic regime of the grain settling. Note that for the jet erosion configuration is used sometimes a so-called “Erosion parameter” corresponding to the square root of the Shields number.<sup>9–11</sup> We have shown recently that the local Shields number, based on self-similar jet models, allows the accurate prediction of the erosion threshold of a model granular bed for both laminar and turbulent impinging plane jets.<sup>15</sup> Above erosion threshold the crater depth has been reported by some recent studies to increase in time before reaching an asymptotic final value.<sup>13,18</sup>

In this paper, we focus on the final crater shape and we describe the different crater morphologies in terms of the Shields number for a turbulent round gas jet impinging a model granular bed. Section II describes the experimental set-up and the different observed morphologies. In section III, the evolution of the crater characteristics — depth, radius, volume, end slope and aspect ratio — are reported as a function of the Shields number for the two first morphologies. The influence of the granular bed thickness is considered in Section IV for the analysis of the third morphology before the results are discussed in terms of local erosion process in Section V.

## II. EXPERIMENTAL SETUP AND CRATER MORPHOLOGY

The experimental set-up shown in Fig. 1 is made of a vertical round gas jet impinging onto a horizontal granular bed. This granular bed consists in sieved glass beads of diameter  $d = 250 \pm 50 \mu\text{m}$  and density  $\rho_p = 2.5 \times 10^3 \text{ kg/m}^3$  poured into a cylindrical container of diameter 170 mm and height 30 mm with a bottom wall of typical roughness 100  $\mu\text{m}$ . To achieve reproducible results, we first put the grains in excess and gently stirred them before

leveling the granular bed with a ruler to obtain a smooth flat surface of height  $h$ . The vertical position of the bottom wall relative to the cylindrical side wall of the container is varied thanks to wedges of different thicknesses so that the height  $h$  of the granular bed lies in the range  $5 \leq h \leq 30$  mm ( $20 \leq h/d \leq 120$ ). The jet of gas originates from a Nitrogen pressured bottle and flows out by a straight cylindrical tube of length  $L = 200$  mm and internal diameter  $D = 4$  mm at the atmospheric ambient pressure and ambient temperature with a density  $\rho \simeq 1.2 \text{ kg/m}^3$  and a viscosity  $\eta \simeq 1.66 \times 10^{-5} \text{ Pa} \cdot \text{s}$ . The bottom end (outlet) of this vertical tube corresponding to the physical origin of the jet is at a distance  $l$  above the horizontal granular bed. This distance  $l$  has been varied in the range  $5 \lesssim l \lesssim 12$  cm corresponding to a dimensionless jet/bed distance  $l^* = l/D$  in the range  $10 \lesssim l^* \lesssim 30$ . The tube is aligned with the axis of the cylindrical container so that the jet impinges at the center of the granular bed. The flow rate  $Q$  measured with a flow meter just upstream the tube has been varied using an adjusting valve up to the maximal value  $3 \text{ cm}^3/\text{s}$  corresponding to a mean velocity of the jet flow  $U_J = 4Q/\pi D^2$  at the tube outlet up to  $24 \text{ m/s}$  with an accuracy of about  $0.2 \text{ m/s}$ . The maximum Reynolds number of the jet is thus  $Re_J = \rho U_J D/\eta \simeq 7 \times 10^3$ . As the Reynolds number of the flow satisfies the conditions  $Re_J \gg L/D$  and  $Re_J \gg 10^3$ , there is a plug flow at the tube outlet and the jet is in a turbulent regime. In the present jet erosion situation, the relevant dimensionless parameter is the global inertial Shields number based on the typical jet velocity  $U_J$  at the tube outlet  $Sh_J = \rho U_J^2 / (\rho_s - \rho)gd$ .<sup>15</sup> This dimensionless parameter compares the inertial fluid forces of the jet to the apparent gravity forces of the grains. All the physical parameters involved in  $Sh_J$  are kept constant in the present experiments except the jet velocity  $U_J$  so that the variations of  $Sh_J$  are directly related to the variations of  $U_J$ . The procedure of a typical experiment of jet cratering is the following. The jet flow is adjusted to the prescribed value but first stopped by an horizontal plate located between the granular bed and the tube outlet. This plate is then removed quickly at a time that corresponds to the time origin  $t = 0$  of the experiment. At time  $t \geq 0$ , the jet impacts the granular bed with the constant jet velocity  $U_J$  and a possible crater hole may form progressively in the granular bed before reaching a quasi stationary state. In this paper we only characterize the steady crater shapes that are reached at long enough time. Note that these stationary shapes correspond to a dynamical equilibrium and can relax and be modified when the jet is stopped.

The shape of the crater is measured from above along one diameter using a laser pro-

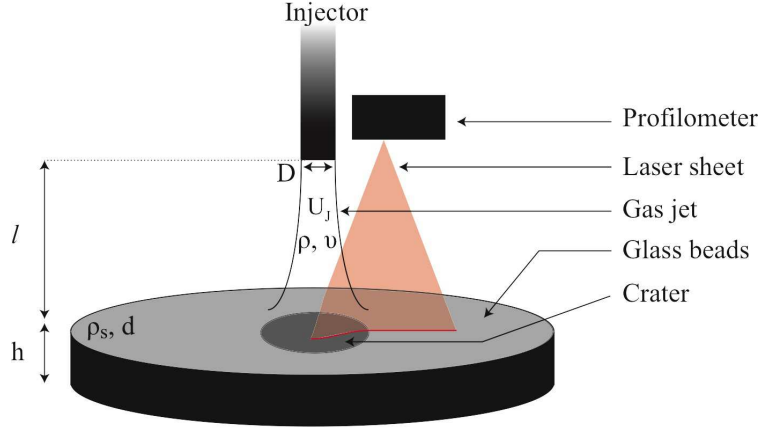


FIG. 1: Sketch of the experimental setup.

filometer with a raw length of 1280 pixels located such that the laser sheet contains the jet axis (Fig. 1). Instantaneous height measurements of the granular bed  $\xi(r, t)$  are recorded at the frequency  $f = 25$  Hz along the radial position  $r$ , where  $r = 0$  corresponds to the jet axis. The vertical precision is about  $20 \mu\text{m}$  while the radial resolution is about  $50 \mu\text{m}$  for a working distance of about 10 cm between the profilometer and the granular bed. The measurements are made along one given diameter which is not restrictive as we ensure visually that the crater remains axisymmetric in the present experiments. In order to be sure that we capture the maximum depth of the crater at the jet axis, the measurements are made along a radial length of about 10 cm that does not originate from  $r = 0$  but is slightly shifted by a small value of about 1 cm such that  $r$  is typically in the range  $-1 \lesssim r \lesssim 9$  cm. In the stationary state, at long enough time ( $t \rightarrow \infty$ ), a time average of the height profile of the surface,  $\xi_\infty(r) = \langle \xi(r, t) \rangle_t$ , is made over about 100 successive profiles to reduce the noise. Before the jet impacts the granular bed ( $t < 0$ ), we measure the average height profile of the initial granular surface  $\xi_0(r) = \langle \xi(r, t) \rangle_t$  and the crater depth profiles  $p(r)$  presented in the following correspond to the difference  $p(r) = \xi_0(r) - \xi_\infty(r)$  between the averaged initial and final height profiles.

Different types of craters are observed depending on the jet velocity and the jet-bed distance above the erosion threshold (fig. 2). Slightly above the erosion threshold  $Sh_c$ , the crater profile, denoted I, presents a parabolic shape with a maximum crater depth  $P_0$  and a crater radius  $R_0$ . The two corresponding crater sizes  $P_0$  and  $R_0$  are given by the best parabolic fit of the experimental data. The maximum crater depth is always close to the

jet axis ( $P_0 \simeq p(0)$ ) so that the crater profile satisfies the relation  $p(r) = P_0 [1 - (r/R_0)^2]$ . Using this definition, the crater radius  $R_0$  corresponds to the radial extent of the crater relatively to the initial bed surface  $p(r) = 0$  and does not take into account the possible external rim of deposited grains at  $r > R_0$  above the initial bed surface. In the same way, the crater depth  $P_0$  corresponds to the depth relative to the initial bed surface  $p(r) = 0$ , whatever the possible external rim crest of deposited grains is. For this crater shape, the end slope of the crater is  $\theta_0 = -dp/dr|_{r=R_0} = 2P_0/R_0$ . This parabolic crater shape will be referred as type I and correspond to the so called Weakly Deflected Jet Regime.<sup>11</sup> The time evolution of such parabolic crater has been analyzed in details by Sutherland and Dalziel,<sup>13</sup> with a linear time evolution of the crater depth before saturation.

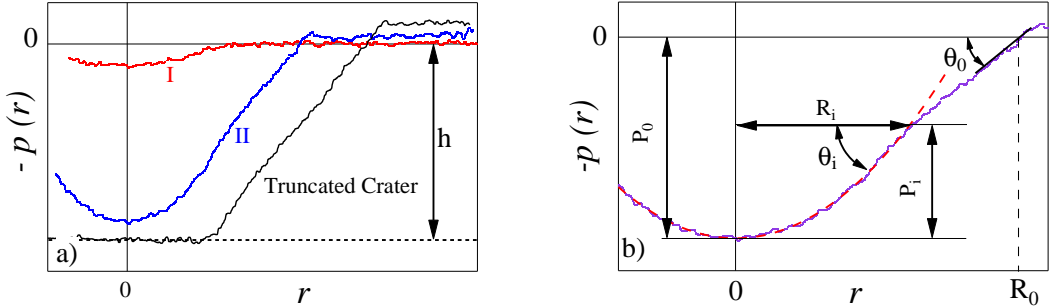


FIG. 2: a) Crater shapes  $p(r)$  for a jet/bed distance  $l^* = 28.8$  and increasing Shields number  $Sh_J$  corresponding to a crater of type I ( $Sh_J = 62$ , —), a crater of type II ( $Sh_J = 84$ , —) and a truncated crater ( $Sh_J = 105$ , —). The horizontal dotted line corresponds to the bottom wall ( $p = h = 20$  mm) of the container. b) Sketch of the different crater parameters.

Further above the erosion threshold  $Sh_c$ , we observe a deeper and wider crater, with larger values of  $P_0$  and  $R_0$ , but with a profile  $p(r)$  separated in two different parts in curves. Indeed, a parabolic part remains close to the jet axis until to an intermediate radius  $R_i < R_0$  while a straight part develops at larger radial extend for  $R_i \leq r \leq R_0$  and thus forms a conical part. This part of the crater profile is well fitted by a linear law  $p(r) = \theta_0(R_0 - r)$  where the end slope value  $\theta_0$  in the range  $R_i \lesssim r \lesssim R_0$ . The inner parabolic part of relative depth  $P_i < P_0$  is thus now given by the relation  $p(r) = (P_0 - P_i) + P_i [1 - (r/R_i)^2]$  for  $r \leq R_i$ . This crater shape with two parts will be referred as type II and corresponds to a Strongly Deflected Jet Regime.<sup>9,11</sup> The time evolution of the depth of such craters has been reported

to be logarithmic.<sup>12,18</sup>

At large enough jet flow, the bottom wall of the cell affects the crater and the maximum depth saturates at the initial granular depth value  $h$  in a central part that extends up to a radius  $R_f$ . In such a case, the crater presents a flat bottom in the central part of equation  $P_0 = h$  for  $r \leq R_f \leq R_i$  (or  $R_0$ ) and a straight outer part of equation  $p(r) = \theta_0(R_0 - r)$  for  $R_i \leq r \leq R_0$  which forms by axisymmetry a truncated conical part. These horizontal and inclined part are connected in between the two neighbouring radius  $R_f$  and  $R_i$  by a small parabolic part. By axisymmetry this forms a small parabolic crown connecting the inner flat part to the outer truncated conical part. This truncated crater shape with an inner flat part does not come from the interaction of the jet flow with the granular material only but from the finite thickness of the granular bed. Strictly speaking, this is thus not a third intrinsic type of crater.

In the following we characterize the evolution of the geometrical parameters of the craters, represented in Fig. 2b, as a function of the Shields number. We first focus on the global parameters of the craters defined for the different types: The crater depth and radius  $P_0$  and  $R_0$ , the slope  $\theta_0$  at the crater periphery, the volume of the eroded crater  $V_0 = \int_0^{R_0} p(r)2\pi r dr$ , and the aspect ratio  $P_0/R_0$  of the crater. The transition between the craters of types I and II can be clearly seen in the evolution of these parameters. We then focus on the evolution of the intermediate parameters of craters of type II : The intermediate depth  $P_i$  and radius  $R_i$  that connect the central parabolic part to the outer straight part. The volume of the parabolic part of the crater defined as  $V_i = \int_0^{R_i} [p(r) - P_i]2\pi r dr$  and the end slope of this parabolic part  $\theta_i = -dp/dr|_{r=R_i}$  are also of interest. All these global and intermediate parameters are discussed first in relation with the global Shields number based on the typical jet velocity  $U_J$  at the injector outlet, but ultimately with the local Shields number  $Sh_l$  based on the local jet velocity close to the granular surface. As a matter of fact, this local Shields number has been shown to govern the erosion threshold in the similar configuration of a plane liquid jet impinging a liquid immersed granular bed in both laminar and turbulent regimes.<sup>15</sup>

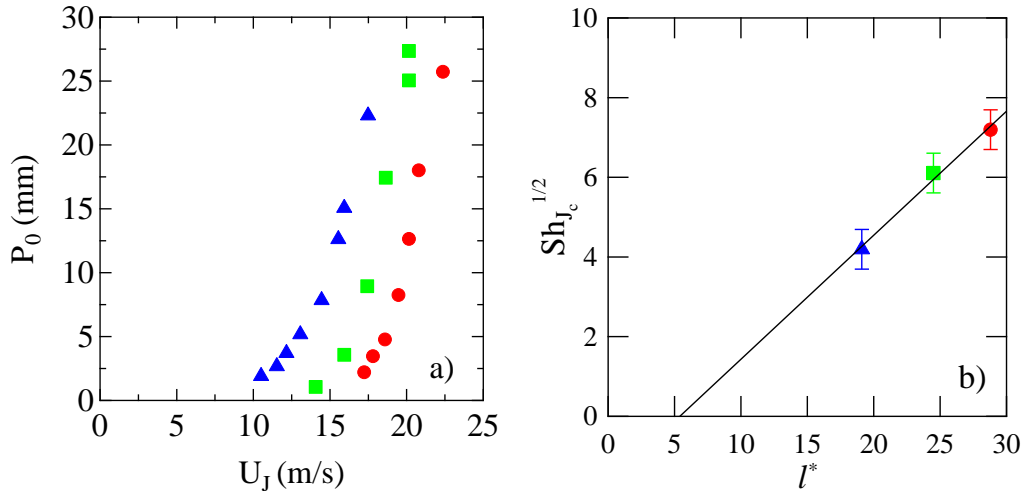


FIG. 3: (a) Crater depth  $P_0$  as a function of the jet velocity  $U_J$  for three dimensionless jet-bed distance  $l/D = 19.1$  ( $\blacktriangle$ ),  $24.5$  ( $\blacksquare$ ),  $28.8$  ( $\bullet$ ) but a given bed thickness  $h/d = 120$ . (b) Corresponding (square root) critical Shields number  $Sh_{J_c}^{1/2}$  for erosion threshold as a function of  $l^* = l/D$ . (—) Linear fit through the data of equation  $Sh_{J_c}^{1/2} = 0.3(l^* - 6)$ .

### III. FROM SHALLOW PARABOLIC TO DEEP CONICAL CRATERS: TRANSITION I/II

Before showing the cratering results in terms of dimensionless parameters, we first consider the resulting final crater depth  $P_0$  as a function of the jet velocity  $U_J$  in Fig. 3a for three values of the jet-bed distance  $l^* = l/D$ . For each value of  $l$ ,  $P_0$  increases with  $U_J$  provided that the bottom wall is not reached (here  $P_0 < 3$  cm), and there exists a critical value  $U_{J_c}$  below which no crater forms. This critical value  $U_{J_c}$  of erosion increases with  $l$ :  $U_{J_c} = 9.5 \pm 0.5$  m/s,  $14 \pm 0.5$  m/s, and  $16.5 \pm 0.5$  m/s for  $l^* \simeq 19.1$ ,  $24.5$  and  $28.8$ , respectively. Conversely, for a given value of  $U_J$ ,  $P_0$  decreases for increasing  $l$ , and there exists a critical value,  $l_c$ , above which no crater forms as no erosion arises. The critical velocity  $U_{J_c}$  measured experimentally leads to the corresponding critical Shields number for erosion,  $Sh_{J_c}$ , which is expected to be function of both the flow regime and the jet-bed distance as demonstrated by Badr *et al.*<sup>15</sup> In the present experiments, for large values of Re to reach the turbulent regime and large enough  $l^*$ ,  $Sh_{J_c}$  is expected to be a strictly increasing function of  $l^*$  which is what we observe here. Following a recent analysis of the jet erosion threshold,<sup>15</sup> we consider that the jet flow is well described by an axisymmetric self-similar

model of free turbulent jet for the range of  $l^*$  explored in the present study. In the stream-wise direction  $x$  downstream from the tube outlet ( $x = 0$ ), i.e. at dimensionless distances  $x^* = x/D$  larger than about 15,<sup>19</sup> the axial velocity  $u(x)$  of the jet can be described by the self-similar axisymmetric law  $u(x)/U_J = K/(x^* + \lambda^*)$ , where  $K$  is the velocity decay rate and  $\lambda^* = \lambda/D$  is the dimensionless distance of the virtual origin from the outlet, with here a positive (resp. negative) value for a virtual origin located upstream (resp. downstream) of the outlet. Considering that the local Shields number  $Sh_l$  evaluated at the undeformed flat bed surface ( $x^* = l^*$ ) should be constant,<sup>15</sup>  $Sh_{J_c}^{1/2}$  should thus scale linearly with  $l^*$ . This is what is observed in Fig. 3b. The extrapolation of a linear fit through the data leads to the virtual origin  $\lambda^* = -6 \pm 0.5$ . The negative value of  $\lambda^*$  means that the virtual origin is here downstream from the tube outlet. This is expected even if the sign and the accurate value of  $\lambda^*$  together with the  $K$  value depend largely on the range of Reynolds number, on the range of  $x^*$  and on the nozzle geometry.<sup>14</sup> In the present range of Reynolds numbers, the corresponding attenuation rate is expected to be around  $K \simeq 4$ .<sup>20</sup>

In the self-similar description, the relevant characteristic length scale of the flow and thus its erosive action should be no more  $l$  or  $D$  but is  $l + \lambda$ . The crater depth and width presented in the following will thus be made dimensionless using the length scale  $l + \lambda$  and studied first as a function of the global Shields number  $Sh_J$  prior to consider the local Shields number  $Sh_l$ .

The crater dimensionless depth  $\tilde{P}_0 = P_0/(l + \lambda)$  is plotted in Fig. 4a as a function of the deviation of the Shields number from its critical value for erosion  $Sh_J - Sh_{J_c}$ . All data points of Fig. 3a now collapse onto a single master curve in Fig. 4a. It means that the variation with  $l$  of the erosive strength of the jet outflow, characterized by  $Sh_J$ , is now described by  $Sh_{J_c}$ . In the evolution of  $\tilde{P}_0$  with  $Sh_J - Sh_{J_c}$  reported in Fig. 4a, we observe two different behaviors:  $\tilde{P}_0$  first increases linearly with  $Sh_J - Sh_{J_c}$  for  $\tilde{P}_0 \lesssim 0.1$  and  $Sh_J - Sh_{J_c} \lesssim 20$  before a strong non linear increase close to  $(Sh_J - Sh_{J_c})^{3/2}$ . The departure from a linear behavior of  $\tilde{P}_0$  vs  $Sh_J - Sh_{J_c}$  is related to a transition in the crater morphology, as now shown in Fig. 4b,c,d by the analysis of the corresponding evolution with  $Sh_J - Sh_{J_c}$  of the dimensionless radius  $\tilde{R}_0 = R_0/(l + \lambda)$  of the crater, its dimensionless volume  $\tilde{V}_0 = V_0/(l + \lambda)^3$  and its end slope  $\theta_0 = -dp/dr|_{R_0}$ .

An important point is that the crater radius remains constant around the typical value  $\tilde{R}_0 \simeq 0.3$  (Fig. 4b) while  $\tilde{P}_0$  increases linearly with  $Sh_J - Sh_{J_c}$ . The crater end slope  $\theta_0$

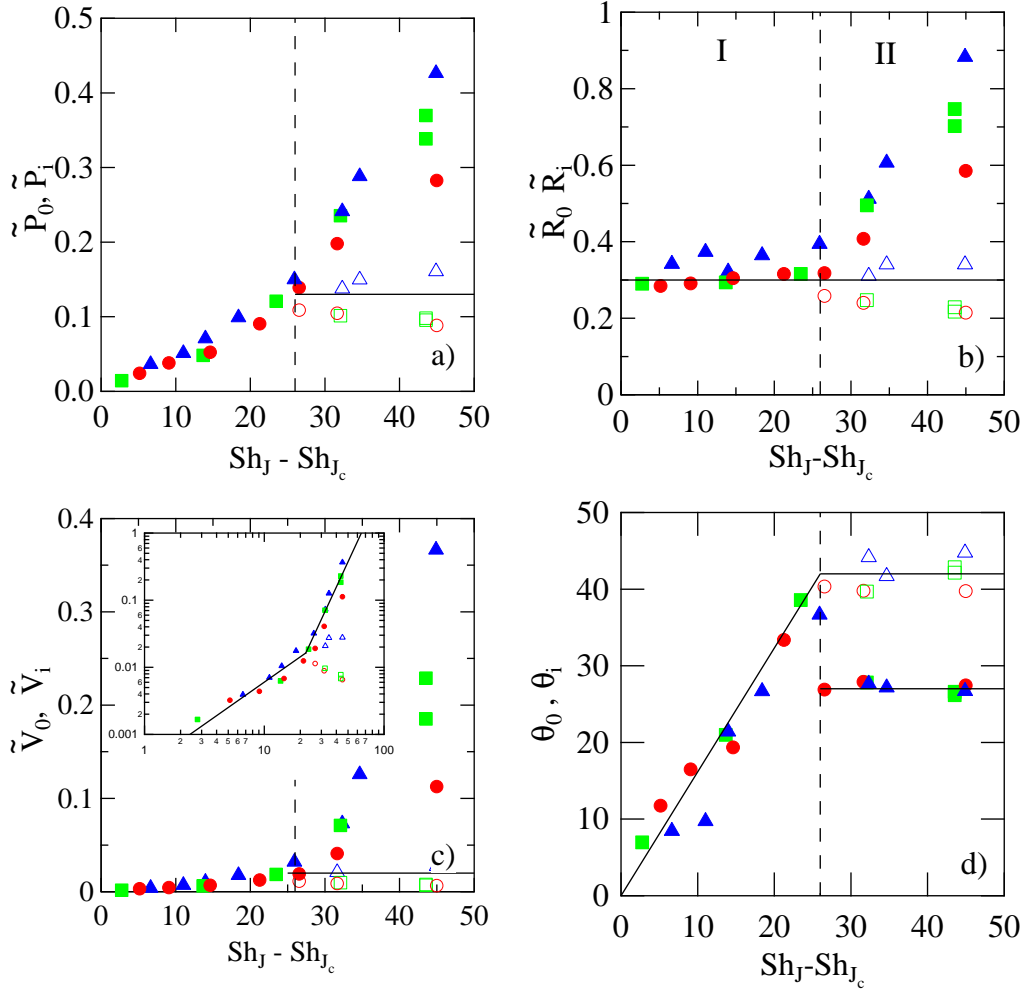


FIG. 4: Evolution of the crater morphology as a function of the Shields number deviation from erosion threshold  $Sh_J - Sh_{J_c}$ : (a) dimensionless crater depth  $\tilde{P}_0$ , (b) crater radius  $\tilde{R}_0$ , (c) crater volume  $\tilde{V}_0$  and (d) crater end slope  $\theta_0$ . Same filled data symbols as in Fig. 3 together with open data symbols corresponding to the internal crater parameters (a)  $\tilde{P}_i$ , (b)  $\tilde{R}_i$ , (c)  $\tilde{V}_i$  and (d)  $\theta_i$ . The vertical dashed line in each plot corresponds to

$$Sh_{J_{cII}} - Sh_{J_c} = 26 \text{ for the transition I/II.}$$

thus increases linearly with  $Sh_J - Sh_{J_c}$  up to about  $40^\circ$  for  $Sh_J - Sh_{J_c} \simeq 26$  (Fig. 4d). The transition I/II in the crater morphology can be observed in Fig. 4d as  $\theta_0$  decreases abruptly by more than  $10^\circ$  near  $Sh_J - Sh_{J_c} \simeq 26$  and then remains constant with a mean value of  $\theta_0 = 27^\circ \pm 2^\circ$ . The transition I/II corresponds to the appearance of granular avalanches on the crater slope. The largest value  $\theta_0 \simeq 40^\circ$  just below the transition I/II corresponds to the maximum angle of stability  $\theta_m$ , i.e. the avalanche starting angle. The critical value  $\theta_0 \simeq 27^\circ$

corresponds to the angle of repose  $\theta_r$ , i.e. the avalanche stopping angle, which is here a little larger than the value reported for such grains in classical avalanche experiments.<sup>21</sup> This slightly larger value of the angle of repose comes from two geometrical factors: (i) a stabilizing inner conical shape and (ii) a small pile length ( $R_0 - R_i \lesssim 10^2 d$ ). The maximum angle of stability found here,  $40^\circ$ , is by contrast much larger than the usual values.<sup>21</sup> This large value is due to the high stabilizing effect of the backward jet flow: It undoubtedly delays the avalanche start in the type I crater shape. Indeed it was shown that the avalanche slope angle increases linearly with the Shields number in a laminar parallel flow situation of upwards water flows above an inclined granular bed.<sup>22</sup> As the first avalanche starts, the backward jet flow changes abruptly from a “smooth” flow attached to the entire crater slope towards a “strong” detached flow with a backward flow now restricted to the inner parabolic part of the crater whereas a weak recirculating flow now takes place along the outer crater side. These flow descriptions correspond to the Weakly and Strongly Deflected Jet Regimes introduced by Aderibigbe.<sup>11</sup> This abrupt change of the flow induced by the avalanche process is in turn responsible for the very large relaxation of  $\theta_0$  that corresponds here to an unusual value,  $\theta_m - \theta_r \simeq 10^\circ$ , much larger than the usual value  $3^\circ$ .<sup>21</sup>

For the crater of type I, as  $\tilde{P}_0$  increases linearly with  $Sh_J - Sh_{J_c}$  while  $\tilde{R}_0$  is constant, the dimensionless volume  $\tilde{V}_0 = (\pi/2)\tilde{P}_0\tilde{R}_0^2$  of the corresponding parabolic crater shape increases linearly with  $Sh_J - Sh_{J_c}$  as shown in Fig. 4c. For  $Sh_J - Sh_{J_c} \gtrsim 26$ , i.e., for the type II regime, the crater radius  $R_0$  is not constant anymore but now increases with  $Sh_J - Sh_{J_c}$  in close relation with the crater depth  $P_0$ . Indeed, the end slope angle  $\theta_0 \sim \tan^{-1}(2P_0/R_0)$  is constant in this regime and is governed by the avalanche process. Therefore, the crater volume  $\tilde{V}_0$  increases faster with respect to  $Sh_J - Sh_{J_c}$ , with a scaling law  $\tilde{V}_0 \sim (Sh_J - Sh_{J_c})^{9/2}$  as  $\tilde{P}_0$  and  $\tilde{R}_0$  both scale as  $(Sh_J - Sh_{J_c})^{3/2}$  in this regime. Note that this large cratering volume is thus not so much related to erodibility but much more to avalanche process.

To summarize the crater evolution from type I to type II, the global aspect ratio  $P_0/R_0$  of the crater is the relevant parameter as shown in Fig. 5. In the type I regime, slightly above the erosion threshold, for  $Sh_J - Sh_{J_c} \lesssim 26$ ,  $P_0/R_0$  increases linearly with  $Sh_J - Sh_{J_c}$  in the same way as  $P_0$  since  $R_0$  is constant. In the type II regime, for  $Sh_J - Sh_{J_c} \gtrsim 26$ ,  $P_0/R_0$  tends towards a limit value  $\tan \theta_0 \simeq 0.5$  corresponding to a critical avalanche slope angle  $\theta_0 \simeq 27^\circ$ .

After characterizing the evolution of the global parameters of the craters of types I and II,

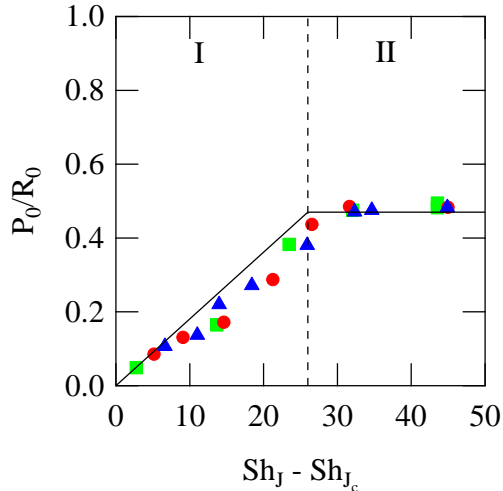


FIG. 5: Aspect ratio  $P_0/R_0$  of the crater as a function of the Shields number deviation,  $Sh_J - Sh_{J_c}$ . Same data symbols as in Figs 2 and 3. The vertical dashed line of equation  $Sh_{J_{cII}} - Sh_{J_c} = 26$  corresponds to the transition I/II. The continuous lines correspond to the linear fit  $P_0/R_0 \simeq 0.018(Sh_J - Sh_{J_c})$  in regime I, and to the constant value

$$P_0/R_0 \simeq 0.47 \text{ in regime II.}$$

we now focus on the internal parameters related to the parabolic part of the craters of type II. In this regime,  $P_i$  and  $R_i$  correspond to the relative depth and radius of the parabolic shape, respectively,  $V_i$  to the volume and  $\theta_i = -dp/dr|_{R_i}$  to the end slope. The evolution of the dimensionless parameters  $\tilde{P}_i = P_i/(l + \lambda)$ ,  $\tilde{R}_i = R_i/(l + \lambda)$ ,  $\tilde{V}_i = V_i/(l + \lambda)^3$  and  $\theta_i$  as a function of  $Sh_J - Sh_{J_c}$  is reported with open data symbols in Fig. 4. The main point is that all these parameters that describe the parabolic shape remain constant above the transition I/II, i.e. for  $Sh_J - Sh_{J_c} \gtrsim 26$ :  $\tilde{P}_i = 0.13 \pm 0.03$ ,  $\tilde{R}_i = 0.3 \pm 0.1$ ,  $\tilde{V}_i = 0.03 \pm 0.01$  and  $\theta_i = 42^\circ \pm 2^\circ$ . It means that the parabolic part remains the same in the cratering process even if the crater of type II is globally deeper and wider with increasing  $\tilde{P}_0$  and  $\tilde{R}_0$  when increasing  $Sh_J - Sh_{J_c}$ . This invariant parabolic shape, present at the eroding jet head, thus corresponds to the final shape of the parabolic crater of type I at the transition I/II. The real jet erosion process takes only place in this small parabolic region that has reached its final invariant shape. For all craters of type II composed of an inner parabolic and an outer conical part, there is always the same discontinuity of the local crater slope  $dp/dr$  that jumps from the large value  $\theta_i \simeq 40^\circ$  to the lower value  $\theta_0 \simeq 27^\circ$  at the connection point ( $r = R_i$ ) between the two regions. This slope discontinuity is associated to the detachment of the

backward jet flow at this point between the inner parabolic shape and the outer conical shape.

To summarize, the jet erosion begins with a shallow parabolic cratering of constant radius that deepens progressively causing an increase of the end slope up to a critical value where avalanche arises and backward flow detaches. The crater of type I then turns out to type II with an invariant inner parabolic head of constant radius and depth that progresses downwards with an increasing outer conical part of constant avalanche slope. In the following section we see how this evolution is modified by the presence of a solid bottom wall.

#### IV. INFLUENCE OF GRANULAR BED THICKNESS

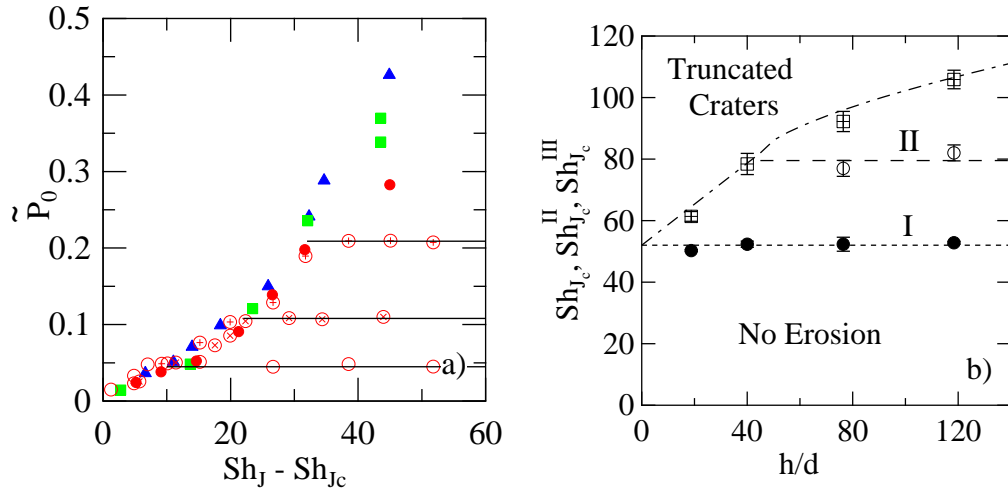


FIG. 6: (a) Dimensionless crater depth  $\tilde{P}_0$  as a function of the Shields deviation from erosion threshold  $Sh_J - Sh_{Jc}$  for a given dimensionless distance between the jet and the granular bed,  $l^* = 28.8$ , and three different values of the bed thickness,  $h/d = 80$  ( $\oplus$ ),  $h/d = 40$  ( $\otimes$ ), and  $h/d = 20$  ( $\circ$ ), together with the data of Fig. 4a for  $h/d = 120$  and different values of  $l^*$ . (b) Critical Shields numbers  $Sh_{Jc}$  for erosion threshold ( $\bullet$ ),  $Sh_{Jc}^{II}$  for transition I/II ( $\circ$ ) and  $Sh_{Jc}^T$  for the appearance of truncated craters ( $\boxplus$ ), as a function of the bed thickness  $h/d$ .

We here focus on the influence of the granular bed thickness  $h$  on the cratering processes. The experiments at different bed thicknesses in the range  $20 < h/d < 120$  have been performed at a fixed jet-bed distance of  $l^* = 28.8$ . The evolution of the dimensionless crater depth  $\tilde{P}_0$  as a function of  $Sh_J - Sh_{Jc}$  is shown in Fig. 6a:  $\tilde{P}_0$  increases with  $Sh_J - Sh_{Jc}$

until it reaches a limit value corresponding to  $P_0 = h$  when there is no more grains at the bottom. The main point is that  $\tilde{P}_0$  follows the same master curve when varying  $Sh_J - Sh_{J_c}$  for all the bed thickness  $h/d$  considered in this study, provided that the bottom of the cell is not reached. The deviation from this master curve at  $P_0 = h$  is not smooth but abrupt. We thus may conclude that the jet erosion process is only a surface phenomena which is only marginally affected by the deeper grain layers in the bulk. This is confirmed with the measurement of the critical Shields number  $Sh_{J_c}$  shown in Fig. 6b (●). Here,  $Sh_{J_c}$  is constant for the different bed thicknesses with a value  $Sh_{J_c} \simeq 53 \pm 2$ . The transition between craters of type I and craters of type II is also not affected by the bed thickness  $h/d$  with a constant value  $Sh_{J_c}^{II} = 79 \pm 4$  as shown in Fig. 6b (○). This corresponds to the critical value  $Sh_{J_c}^{II} - Sh_{J_c} = 26 \pm 3$  already reported in Section 3 for  $h/d = 120$ . As expected, the critical Shields number  $Sh_{J_c}^T$ , corresponding to the birth of truncated craters, is directly related to the bed thickness  $h$  as shown in Fig. 6b where  $Sh_{J_c}^T$  increases with  $h/d$  and tends to  $Sh_{J_c}$  for vanishing  $h/d$ . When  $Sh_{J_c}^T < Sh_{J_c}^{II}$  which corresponds here to  $h/d \lesssim 45$ , craters of type I become truncated before turning into craters of type II. When  $Sh_{J_c}^T > Sh_{J_c}^{II}$  (here  $h/d \gtrsim 45$ ), craters of type I turn first into craters of type II before being truncated. From the scaling observed for  $\tilde{P}_0$  with  $(Sh_J - Sh_{J_c})$  in Fig. 4a, it is expected that  $Sh_{J_c}^T - Sh_{J_c}$  scales linearly with  $h/d$  at low enough  $h/d$  ( $h/d \lesssim 45$ ), but non linearly with the scaling  $(h/d)^{2/3}$  at high enough  $h/d$  ( $h/d \gtrsim 45$ ). The value  $h/d \simeq 45$  corresponds to the “triple point” separating the three morphologies in Fig. 6b. This value comes from the value  $h/(l + \lambda) \simeq 0.12$  given for the transition I/II from Fig. 4a with here  $l + \lambda = 22.8D$  and  $D/d = 16$ .

Note that the radial extension  $\tilde{R}_f$  of the flat part of the truncated craters is found to increase linearly with  $Sh_J - Sh_{J_c}^T$  at the same rate as  $\tilde{R}_0$  so that the difference  $\tilde{R}_0 - \tilde{R}_f$  remains constant. It means that the eroded grains are expelled beyond  $\tilde{R}_0$  out of the crater. However, the difference  $\tilde{R}_0 - \tilde{R}_f$  depends on  $h/d$  as  $\tilde{R}_0$  will increase either from the value  $\tilde{R}_0 \simeq 0.3$  or from a value  $\tilde{R}_0 > 0.3$  depending on whether truncated craters arise from type I or II. Because the crater depth  $P_0$  is kept constant when  $R_0$  increase, the aspect ratio  $P_0/R_0$  of the truncated craters now decreases when increasing  $Sh_J$ . Truncated craters have thus a slightly different morphology depending on whether they originate from craters of type I or II. In the first case, the inner flat part of radial extension  $R_f$  is followed by an outer annular parabolic part of constant width  $R_0 - R_f \leq R_i$  with an end slope  $\theta_0 \lesssim 40^\circ$ . In the second case, the inner flat part is connected to the outer conical part of constant slope  $\theta_0 \simeq 25^\circ$  by

a small parabolic crown of constant extension. Therefore, the detachment of the backward jet flow remains the same whatever the flat or curved central impinging region of the jet.

## V. LOCAL EROSION PROCESS

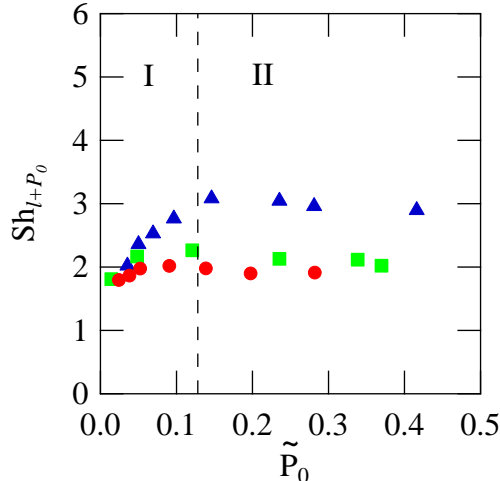


FIG. 7: Local Shields number at the bottom of the crater,  $Sh_{l+P_0}$ , as a function of the dimensionless crater depth  $\tilde{P}_0$  for different jet-bed distance. Same data symbols as in Fig.

3.

In a previous study, we have shown that the jet erosion threshold is governed by the local flow velocity at the bed surface which can be determined using the jet self-similar models.<sup>15</sup> In the present study, we find that the morphology of the craters (except the truncated craters due to finite bed thickness) is entirely controlled by the Shields number deviation from erosion threshold,  $Sh_J - Sh_{J_c}$ , once all the lengths that characterize the crater are made dimensionless by the distance  $l + \lambda$  of the initial flat bed to the virtual origin of the jet. According to these two results, we now look at how the local Shields number  $Sh_{l+P_0}$  based on the local jet flow velocity at the bottom of the crater evolves with the dimensionless depth  $\tilde{P}_0$  of craters in Fig. 7a. As expected from Fig. 3b, the critical local Shields number  $Sh_{l_c}$  corresponding to vanishing  $\tilde{P}_0$  is constant with a value  $Sh_{l_c} \simeq 1.5$ . This value depends on the chosen value for the decay rate of the self-similar model (here  $K \simeq 4$ ) and is very similar to the value  $Sh_{l_c} \simeq 1.2$  found for a plane liquid jet in both laminar and turbulent regime.<sup>15</sup> These result show that the local erosion process is the same for different types of jet (round or plane, gas or liquid, turbulent or laminar). We also observe that  $Sh_{l+P_0}$

remains constant in the type II regime as the cratering head still corresponds to an inner invariant parabolic shape. It means that the local Shields number  $Sh_{l+P_0}$  depends on the curvature of the crater and thus increases with the depth in the type I regime before keeping a constant value related to the jet-bed distance for craters of type II.

This behavior may be explained by the topological change of the crater as it deepens. Indeed  $Sh_{l+P_0}$  has been calculated assuming an unperturbed jet velocity obtained from a free jet self similar model. This is clearly not the case once a crater is formed, as the jet is then affected by the evolving surface profile. Because of the back flow, it is thus expected that the axial velocity given by a self-similar model and used to calculate  $Sh_{l+P_0}$  is overestimated. In the first stage of erosion, crater of type I deepens but keeps a constant outer radius  $\tilde{R}_0$ , so that the back flow increases with the curvature which should induce a local jet velocity decrease. As a consequence  $Sh_{l+P_0}$  inferred from an invariant free jet model should increase. Above transition I/ II, craters of type II keep a parabolic part of constant radius  $\tilde{R}_i$  and constant depth  $\tilde{P}_0 - \tilde{P}_i$  and thus an invariant back flow which leads to a constant  $Sh_{l+P_0}$  however depending on the curvature.

## VI. CONCLUSION

The morphology of the craters resulting from the erosion of a model granular bed by an axisymmetric turbulent gas jet have been studied in detail. Two types of craters depending on the deviation of the Shields number from its critical value for erosion  $Sh_J - Sh_{J_c}$  have been identified and characterized. For small enough  $Sh_J - Sh_{J_c}$  values ( $Sh_J - Sh_{J_c} \lesssim 26$ ), craters of type I have a parabolic profile with a constant radius  $R_0$  but increasing depth  $P_0$  so that the global aspect ratio of the crater  $P_0/R_0$  increases with  $Sh_J - Sh_{J_c}$ . This process leads to an increase of the crater end slope  $\theta_0$  with  $Sh_J - Sh_{J_c}$  up to a critical value at which it relaxes abruptly by about  $10^\circ$  because of avalanche process. This process leads to the birth of craters of type II that are now formed by an invariant inner parabolic part and an outer conical part of invariant end slope. This invariant inner parabolic part means that the jet erosion process remains the same in this cratering regime. For these type II craters, the depth and radius of the crater increases with  $Sh_J - Sh_{J_c}$  in a similar way so that the global aspect ratio of the crater remains constant and governed by the dynamical avalanche slope. Finally, truncated craters appear for a finite bed thickness when the erosion process reaches

the bottom wall. In this case, the crater depth remains of course constant when its radius still increases with  $Sh_J - Sh_{J_c}$  so that the global aspect ratio now decreases with increasing  $Sh_J$ . The analysis performed using a self-similar jet model reveals that the local Shields number at the bed surface keeps a constant value when the bed has a constant shape and that this value depends on the exact bed shape. For the undeformed flat initial granular bed, the local Shields number has a constant value of 1.5 at erosion threshold. The local Shields number increases however with increasing crater curvature. This can be understood by the retroaction of the curved surface on the back flow. For type II craters of constant central parabolic shape at the bottom head, the local Shields number is also found constant when the crater deepens. To further improve the understanding of the jet cratering, some detailed local measurements with coupled fluid/grains velocity measurement would be key elements.

The authors thank L. Auffray and R. Pidoux for their help in the design and realization of the experimental setup and A. Postel for preliminary experiments. This work benefits from fruitful discussions and from financial support within the three research projects STABINGRAM (No. 2010-BLAN-0927-01), SSHEAR (No. ANR-14-CE03-0011) and COMIGS (LabEx PALM- ANR-10-LABX-0039) of the ANR French Research Agency.

## REFERENCES

- <sup>1</sup>O. Devauchelle, L. Malverti, E. Lajeunesse, P.-Y. Lagr e, C. Josserand, and K.-D. N. Thu-Lam, “Stability of bedforms in laminar flows with free surface: from bars to ripples,” *Journal of Fluid Mechanics* **642**, 329–348 (2010).
- <sup>2</sup>B. A. Hamm, W. L. West, and G. B. Tatterson, “Sludge suspension in waste storage tanks,” *AIChE Journal* **35**, 1391–1394 (1989).
- <sup>3</sup>L. Biasi, A. de los Reyes, M. Reeks, and G. de Santi, “Use of a simple model for the interpretation of experimental data on particle resuspension in turbulent flows,” *Journal of Aerosol Science* **32**, 1175 – 1200 (2001).
- <sup>4</sup>M. Kissane and I. Drosik, “Interpretation of fission-product transport behaviour in the ph bus {FPT0} and {FPT1} tests,” *Nuclear Engineering and Design* **236**, 1210 – 1223 (2006).

- <sup>5</sup>M. Foster, R. Fell, and M. Spannagle, “The statistics of embankment dam failures and accidents,” *Canadian Geotechnical Journal* **37**, 1000–1024 (2000).
- <sup>6</sup>G. Hanson and K. Cook, “Apparatus, test procedures, and analytical methods to measure soil erodibility in situ,” *Applied Engineering in Agriculture* **20**, 455–462 (2004).
- <sup>7</sup>K. Mazurek, N. Rajaratnam, and D. Segó, “Scour of cohesive soil by submerged circular turbulent impinging jets,” *Journal of Hydraulic Engineering* **127**, 598–606 (2001).
- <sup>8</sup>H. Rouse, “Criteria for similarity in the transportation of sediment,” Scientific group company, 16 (1939).
- <sup>9</sup>N. Rajaratnam and S. Beltaos, “Erosion by impinging circular jets,” *Proc. ASCE, J. Hydr. Div.* **103**, 1191–1205 (1977).
- <sup>10</sup>N. Rajaratnam, “Erosion by plane turbulent jets,” *Journal of Hydraulic Research* **19**, 339–358 (1981).
- <sup>11</sup>O. Aderibigbe and N. Rajaratnam, “Erosion of loose beds by submerged circular impinging vertical turbulent jets,” *Journal of Hydraulic Research* **34**, 19–33 (1996).
- <sup>12</sup>P. Metzger, C. Immer, C. Donahue, B. Vu, R. Latta, and M. Deyo-Svendsen, “Jet-induced cratering of a granular surface with application to lunar spaceports,” *J. Aerospace Eng.* **2** (2009).
- <sup>13</sup>B. R. Sutherland and S. Dalziel, “Bedload transport by a vertical jet impinging upon sediments,” *Phys. Fluids* **26**, 035103–1 : 035103–19 (2014).
- <sup>14</sup>C. Ball, H. Fellouah, and A. Pollard, “The flow field in turbulent round free jets,” *Progress in Aerospace Sciences* **50**, 1 – 26 (2012).
- <sup>15</sup>S. Badr, G. Gauthier, and P. Gondret, “Erosion threshold of a liquid immersed granular bed by an impinging plane liquid jet,” *Physics of Fluids* **26**, 023302 (2014).
- <sup>16</sup>S. Kuang, C. LaMarche, J. Curtis, and A. Yu, “Discrete particle simulation of jet-induced cratering of a granular bed,” *Powder Technology* **239**, 319 – 336 (2013).
- <sup>17</sup>A. Shields, “Anwendung der ähnlichkeits-mechanik und der turbulenz-forschung auf die geschiebebewegung,” *Preussische Versuchsanstalt für Wasserbau und Schiffbau* **26**, 524–526 (1936).
- <sup>18</sup>A. H. Clark and R. Behringer, “Jet-induced 2-d crater formation with horizontal symmetry breaking,” *Granular Matter* **6**, 433–440 (2014).
- <sup>19</sup>E. Ferdman, M. Otugen, and S. Kim, “Effect of initial velocity profile on the development of the round jet,” *Journal of Propulsion and Power* **16**, 676–86 (2000).

- <sup>20</sup>T. Malmström, A. Kirkpatrick, B. Christensen, and K. Knappmiller, “Centerline velocity decay measurements in low velocity axisymmetric jets.” *J. Fluid Mech.* **246**, 363–377 (1997).
- <sup>21</sup>R. Fischer, P. Gondret, and M. Rabaud, “Transition by intermittency in granular matter: From discontinuous avalanches to continuous flow,” *Phys. Rev. Lett.* **103**, 128002 (2009).
- <sup>22</sup>T. Loiseleux, P. Gondret, M. Rabaud, and D. Doppler, “Onset of erosion and avalanche for an inclined granular bed sheared by a continuous laminar flow,” *Physics of Fluids* **17**, 103304 (2005).